

# **Influence of colloidal surface-additivition with surfactant-free laser-generated metal nanoparticles on Nd-Fe-B permanent magnets produced by suction casting**

Jianing Liu<sup>1</sup>, Ying Yang<sup>2</sup>, Franziska Staab<sup>3</sup>, Carlos Donate-Buendia<sup>2,4</sup>, René Streubel<sup>2</sup>, Bilal Gökce<sup>2,4</sup>, Fernando Macarri<sup>1</sup>, Philipp Gabriel<sup>2</sup>, Benjamin Zingsem<sup>2,5</sup>, Detlef Spoddig<sup>5</sup>, Konstantin Skokov<sup>1</sup>, Oliver Gutfleisch<sup>1</sup>, Michael Farle<sup>5</sup>, Stephan Barcikowski<sup>2\*</sup>, Anna Rosa Ziefuss<sup>2</sup>

<sup>1</sup> Functional Materials, Institute of Material Science, Technical University of Darmstadt, 64287 Darmstadt, Germany

<sup>2</sup> Technical Chemistry and Center for Nanointegration Duisburg-Essen (CENIDE), University of Duisburg-Essen, 45141 Essen, Germany

<sup>3</sup> Physical Metallurgy, Institute of Material Science, Technical University of Darmstadt, 64287 Darmstadt, Germany

<sup>4</sup> Materials Science and Additive Manufacturing, School of Mechanical Engineering and Safety Engineering, University of Wuppertal, 42119 Wuppertal, Germany

<sup>5</sup> Faculty of Physics and Center for Nanointegration Duisburg-Essen (CENIDE), University of Duisburg-Essen, 47048 Duisburg, Germany

\* corresponding author: [stephan.barcikowski@uni-due.de](mailto:stephan.barcikowski@uni-due.de)

Keywords:

Magnetic properties

Hard magnets

Additive Manufacturing

Laser ablation in liquid (LAL)

Grain boundary (GB) diffusion

Microstructure

## **Abstract**

The development of new powder feedstocks using nanoparticles (NPs) has the potential to enhance the functionality of as-built parts and overcome the limitations of current additive manufacturing (AM) techniques. This study investigated the impact of magnet microparticle feedstock modification by NPs on the microstructure and functionality of Nd-Fe-B-based permanent magnets made by suction casting. This casting method is known to at least partially mimic the melting and fast solidification steps inherent to metal powder-based AM techniques such as Laser Powder Bed Fusion. Two types of NPs, Ag, and ZrB<sub>2</sub>, were used, and their effects on grain size distribution and dendritic structure were evaluated. Ag NPs resulted in smaller, more uniform grain sizes and increased functionality, but only for loadings > 0.5 monolayers. ZrB<sub>2</sub> resulted in uniformly distributed grain sizes at much lower mass loadings, with even more compact dendritic arms. The results show that feedstock powder surface modification with low melting point metal NPs can improve the microstructure and magnetic properties of permanent magnets produced by AM and highlight the potential of using NPs to develop new powder feedstocks for AM. With this, it provides insights for future research on optimizing materials for AM processes.

## Introduction

Lasers in additive manufacturing offer flexibility in shape design, reduced material loss, and the possibility of industrial-scale production <sup>1,2</sup>. However, although laser systems are becoming increasingly powerful and brilliant, the materials available are often completely inadequate for the processing tasks currently required <sup>3</sup>. In laser-based additive manufacturing (AM), the material variability is limited due to complex sintering and melting mechanisms during processing. This leads to process instabilities, porosities, and other defects in the as-built parts <sup>4</sup>. Therefore, the materials are urgently needed to adapt to these widespread production processes. Due to its throughput and precision, AM will dominate important production processes in the long term.

Powder bed fusion using a laser beam (PBF-LB) is one of the most prominent AM techniques. Here, a laser beam completely melts the metal feedstocks to obtain fully dense parts after solidification <sup>5,6</sup>. However, extremely high solidification rates in the range of  $10^5$  K/s <sup>7</sup> of the molten metal feedstock may lead to micro-cracks, non-equilibrium microstructure with phase segregation, and columnar grain growth, in most cases, will influence the material strength <sup>4,8</sup>. In AlSi10Mg alloys, the fast-cooling rates result in an ultrafine supersaturated Si-rich network inside each grain which positively influences the corrosion behaviour; however, strong residual stresses and microstructural inhomogeneities negatively affect further mechanical properties like ductility and fatigue resistance <sup>5,9,10</sup>. Yet, compared with structural materials (e.g., 316L, AlSi10Mg, and Ti6Al4V), functional materials like shape memory alloys (e.g., Ni-Mn-In or Co-Ni-Ga) or permanent magnets (PM) based on rare earth elements (e.g., Nd-Fe-B) are rarely produced with AM, and further research is necessary to correlate the melting-induced microstructures with the functional read-out in as-built parts <sup>11-13</sup>. The desirable microstructure for high coercivity in, e.g., Nd-Fe-B alloys consists of Nd<sub>2</sub>Fe<sub>14</sub>B grains isolated by a paramagnetic grain boundary phase <sup>14,15</sup>. However, if high thermal gradients occur during re-solidification, a dendritic microstructure may form, negatively affecting magnetic properties <sup>16,17</sup>. Moreover, an uneven distribution of grain size can also have an adverse effect on coercivity <sup>18</sup>. Thus, further research is necessary to fully comprehend the microstructure and optimize manufacturing permanent magnets using advanced techniques. A fundamental research approach already at the beginning of the process chain, the feedstock power, is required <sup>3</sup>. In the past decade, research has shown that using nanoparticles (NPs)

for feedstock modification can address processability limitations and improve the properties of as-built parts <sup>19,20</sup>. Nonetheless, current research on NP-based feedstock modification focuses on non-functional materials, highlighting the need for comprehensive research on such mater, including the entire process chain, powder feedstock, processing, microstructure, and part properties. Here suction casting is an ideal test bench <sup>15</sup>, as it requires only a few grams of feedstocks, allowing the fast processing of different feedstock modifications. The powder is melted and sucked into a water-cooling mold to simulate the high cooling rate of PBF-LB, a similar microstructure, and the same existing phases can be achieved. Hence, suction casting may be employed as a pre-screening method to exclude low-performing powders from further (then kg-scale) PBF-LB testing series.

This study utilized laser-generated Ag and ZrB<sub>2</sub> NPs to modify a rare-earth-based feedstock material. Studies have demonstrated that incorporating Ag into Nd-based magnets can enhance their functional properties after processing with conventional sintering techniques <sup>21</sup>. Since Ag has a lower melting point than Nd-Fe-B, it can rapidly melt and fill in vacant spaces in the loosely packed powder layers of the PBF-LB/M process, resulting in a higher packing density. Moreover, it is known that Ag and Nd form alloys and even intermetallic phases at high temperatures so that high cooling rates may freeze high-temperature phases that contain Ag and Nd. Both the elevated packing density and formation of Ag-containing Nd-based phases may positively influence the magnetic performance (hypothesis 1, Figure 1B). ZrB<sub>2</sub> NPs melt later than the original feedstock mater and are intended to remain solid during the melting of Nd-Fe-B MQP-S and regulate grain growth during re-solidification (hypothesis 2, Figure 1B).

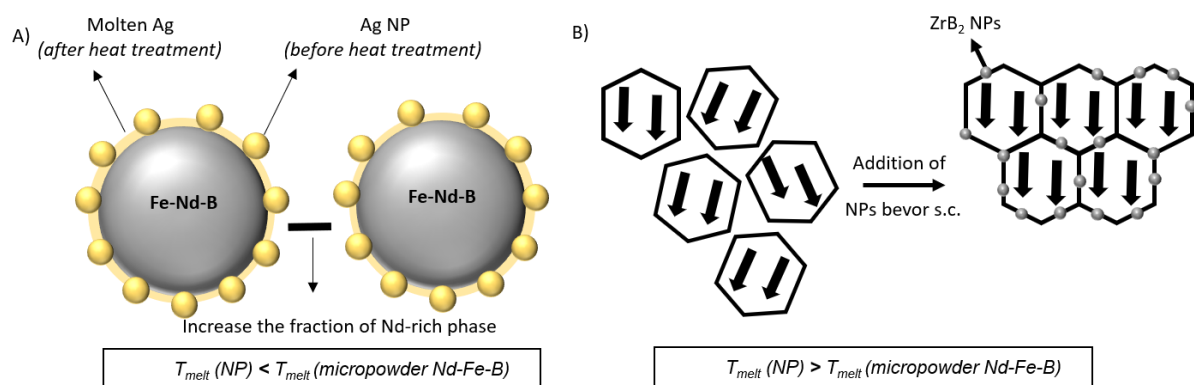


Figure 1 Schematic description of the effect of adding nanoparticles on Nd-Fe-B powder surfaces prior to melting-solidification processing. A) Hypothesis 1: Ag NPs decorated on the surface of Nd-Fe-B microparticles will melt and build Nd-Ag intermetallic

*inclusions in the matrix during solidification, potentially assisting in decoupling the grains. B) Hypothesis 2: ZrB<sub>2</sub> NPs will melt later (or not at all, dependent on process parameters) and resolidify earlier than the Nd-Fe-B, which enables the nanoparticles to act as additional starting points for grain growth, potentially leading to finer, equiaxed grains.*

## **Results and Discussion**

This study investigates the influence of NPs loading on the as-build part microstructure of functional material. We will concentrate on MQP-S, a commercially available permanent feedstock for processing<sup>22,23</sup>. However, strong temperature gradients are expected to reduce the functionality, as unsuitable dendritic microstructures are known to appear after AM processing<sup>23</sup>.

### **Feedstock modification**

The production of NPs was done via laser ablation in liquids, enabling the synthesis of surfactant-free particles<sup>24</sup> without including any cross-effectors on the feedstock powder's flowability<sup>25</sup>. Moreover, cross-effectors like organic residuals or colloidal stabilizers bear the risk of creating gases by laser vaporization. They may cause unwanted balling effects during processing, as has been shown for laser direct-writing of stabilizer-containing Ag microparticle inks<sup>26</sup>. Detailed information on the NPs' production can be found in the method part. Although the particle size in both cases shows a monomodal distribution, the Ag NPs exhibit an average size of 8 nm, while the ZrB<sub>2</sub> NPs have an average size of 100 nm. (Figure 2A). Note that the differences in particle size are intended concerning the different natures of the targeted mechanisms. Hypothesis 1 aims to investigate the impact of an NP "shell" (that is, an NP monolayer), with greater precision in adjusting the shell thickness (fraction of an NP monolayer of multiple layers) achievable when using small Ag NPs. Figure 2B shows the statistical distance between two Nd-Fe-B-based microparticles dependent on the Ag NP's mass loading. Note that NP melting and surface wetting will decrease the effective thickness of the Ag layer on the microparticle surface, resulting in partly lower values.

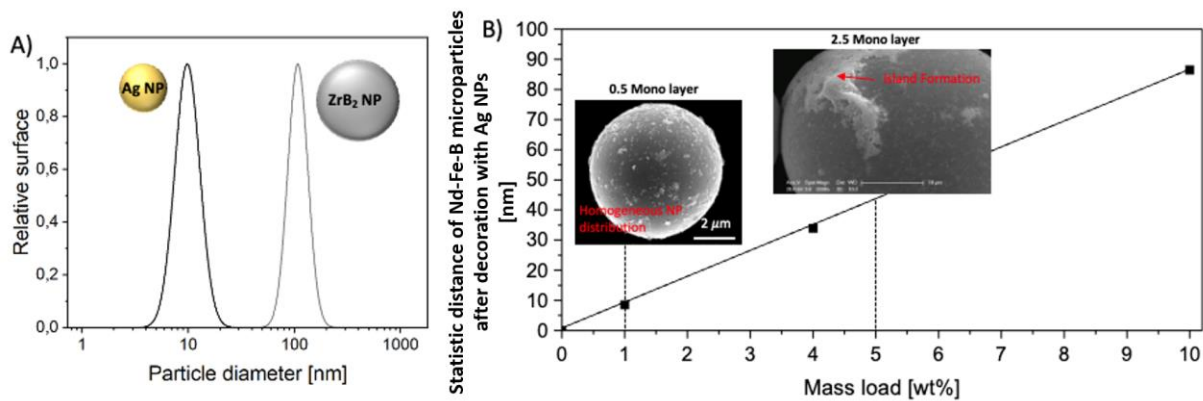


Figure 2: A) Nanoparticle size distribution after laser-based production of Ag NPs (Black) and ZrB<sub>2</sub> NPs (grey) curves. B) Calculated statistical distance of MQP-Smagnet micro powder in dependence on the mass load of Ag NPs. The calculation assumes sphericity for both NPs and MPs and was done using a mean NPs of 8 nm and a mean MPs size of 43 nm (size distribution of the MQP-Smagnet micro powder can be found in the SI).

Hypothesis 2, however, accounts for larger particles to enable strong nucleation sizes. Here, we also varied the NP mass loading on the MP surface, providing the process with a different number of maximal nucleation centers. Here a mass loading of 1wt% would nominally enable 968,000 nucleation centers.

As the Ag NPs were produced in water, we performed the surface decoration electrostatically controlled<sup>27</sup> by simply varying the pH value in the presence of the Ag NPs and Nd-Fe-B MPs. Note that the surface charges are a function of the pH value and that there is a pH range (pH 3-8) where both reagents show an opposite sign of the surface charge (zeta potential is negative for Ag<sup>28</sup> and positive for Nd-Fe-B MPs<sup>29</sup>). However, Nd-Fe-B tends to oxidize in the acidic range<sup>30</sup>, so we carefully adjusted the pH value to 7-8. While lower mass loadings of Ag NPs are highly homogeneously distributed, larger amounts tend to form islands on the microparticle surface (see inset Figure 1B). Additionally, we calculated based on a simplified geometric model<sup>31</sup> that supporting 1 wt% (equivalent to 0.7 Vol%) of Ag NPs on the surface of MQP-S results statistically in a half monolayer of Ag NPs, enabling a statistical distance between two neighboring MPs in the range of the NP's diameter. The ZrB<sub>2</sub> NPs were produced in ethanol. Here, we evaporated the liquid in the presence of the feedstock, increasing the concentration of both agents in time, and promoting adsorption processes by diffusion-controlled deposition.

## Powder processing and characterization of final parts

After successfully modifying the feedstock powder, we processed seven Ag NP-modified feedstock variants (0.1 – 10 wt% loading) and four ZrB<sub>2</sub> modified feedstocks (0.1 – 2 wt% loading) via suction casting, a convenient pre-test bench for PBF-LB<sup>14,15</sup>. As introduced, NPs are known to alter the as-build parts' microstructure, which we characterized using EBSD, SEM-BSE, and SEM-EDX in the following. Note that we performed heat-treatment cycles before further analysis as this causes atomic diffusion and rearrangement of the crystal structure, promoting magnetic anisotropy and coercivity, resulting in stronger functionality<sup>14,32</sup>. Such heat treatments are also widely used in PBF-LB both for microstructural optimization and relief of macro-strain.

Exemplary EBSD images of as-build parts, produced via suction casing, for pure MQP-S and MQP-S additivated with Ag (0.1, 1, and 7 wt%) or ZrB<sub>2</sub> (0.1, and 1 wt%) NPs, are shown in Figure 3. As expected, the microstructure of pure MQP-S suffers significantly from the production conditions (high-temperature gradients and fast cooling rates), resulting in a clearly inhomogeneous grain-size distribution (spots 1 and 2 in Figure 3A) containing grains with sizes far larger than 10 μm. The same applies to samples containing 0.1 and 1 wt.% of Ag (Figure 3 B-C). However, both spots show significantly smaller grains than the unmodified as-build part. The sample containing 7 wt.% of Ag NPs (Figure 3D) and the samples decorated with ZrB<sub>2</sub> NPs (Figure 3E-F) showed a more homogeneous microstructure. In all cases, the grains show a dendritic growth, making it difficult to extract grain size distributions.

In summary, the EBSD results demonstrate a significant impact of NP additivation on the magnet's microstructure, which varies for the two NP materials and is affected by the NP's loading. Raising the Ag NP loading leads to more uniform grain sizes but at the expense of very small grain sizes. Note that the 7 wt% sample possesses an inhomogeneous NP distribution on the feedstock powder (aggregate/island formation) prior to suction casting, for which we cannot exclude any effect of the varied surface dispersion quality on the microstructure of the as-built part, which would be highly interesting to be revealed in future studies. Conversely, increasing the ZrB<sub>2</sub> loading to the same mass leads to a generally good uniformity of grain sizes, with increased size observed at an increased NP mass load.

It is known that there is a correlation between grain size and the functionality of permanent magnets<sup>14</sup>.

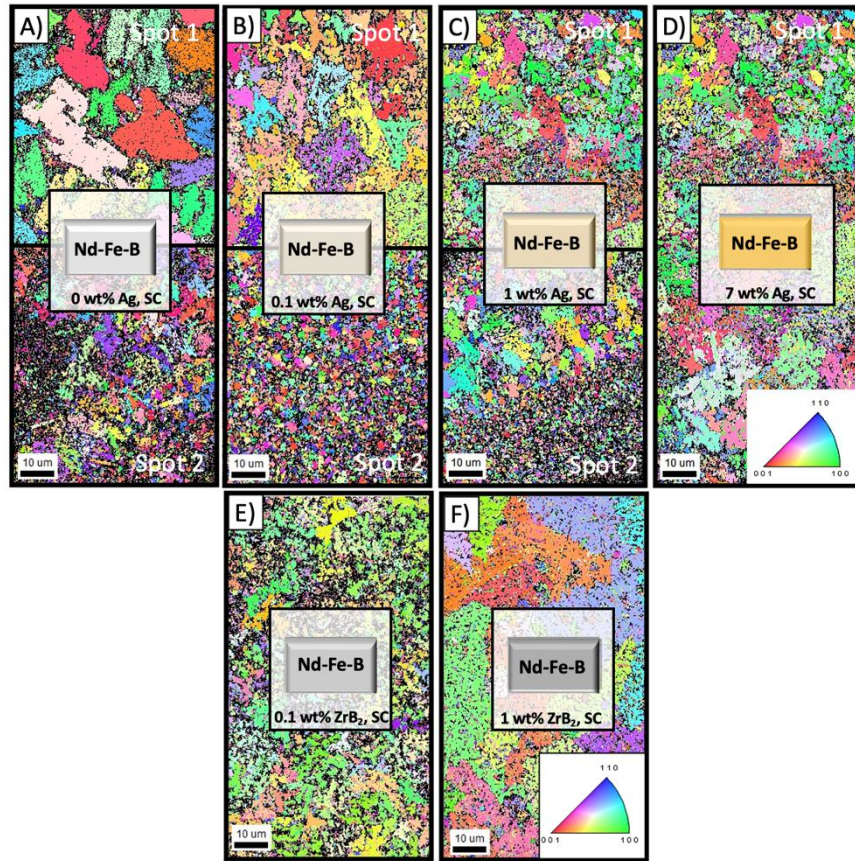


Figure 3 EBSD images of annealed suction casting flakes from (A) non-modified (B-F) and NP-additivated MQP-S powders.

Generally, the grain size closer to single domain size ( $\sim 200$  nm for  $\text{Nd}_2\text{Fe}_{14}\text{B}$ ) lead to the maximal coercivity and optimal remanence<sup>14</sup>. However, there is a trade-off between grain size and other mechanical properties of the material, such as strength and toughness. Therefore, finding the optimal grain size for a given application requires a careful balance of magnetic and mechanical properties which is beyond the scope of the study.

Thus, we performed SEM-BSE to explore how different types of NPs affect grain size. One can see from Figure 4 that instead of small grains separated by a non-magnetic grain boundary phase, the dendritic structure forms in the samples. Dendritic arms are thin, finger-like projections that form during solidification<sup>22,23</sup>. It is known that such dendritic structures can significantly affect the hard magnetic properties of Nd-Fe-B-based alloys<sup>11,33,34</sup>. As shown in Figure 4A, the microstructure of annealed suction-casting flakes from MQP-S powder is dendritic  $\text{Nd}_2\text{Fe}_{14}\text{B}$  surrounded by  $\alpha$ -iron as a grain boundary. Following<sup>33</sup>, the nanocrystalline structure from the raw powder was destroyed during the remelting in the suction casting process, and the microstructure was much coarser afterward. Figure 4B reveals the dendritic



structure for one selected Ag NP-additivated as-built part. The dendritic structure is much finer and more homogeneous, which can also be observed for the ZrB<sub>2</sub>-modified as-built parts. Here, we resolved the dendritic structure for parts with increasing ZrB<sub>2</sub> amount and found the increasing density of dendritic arms with increasing NP content.

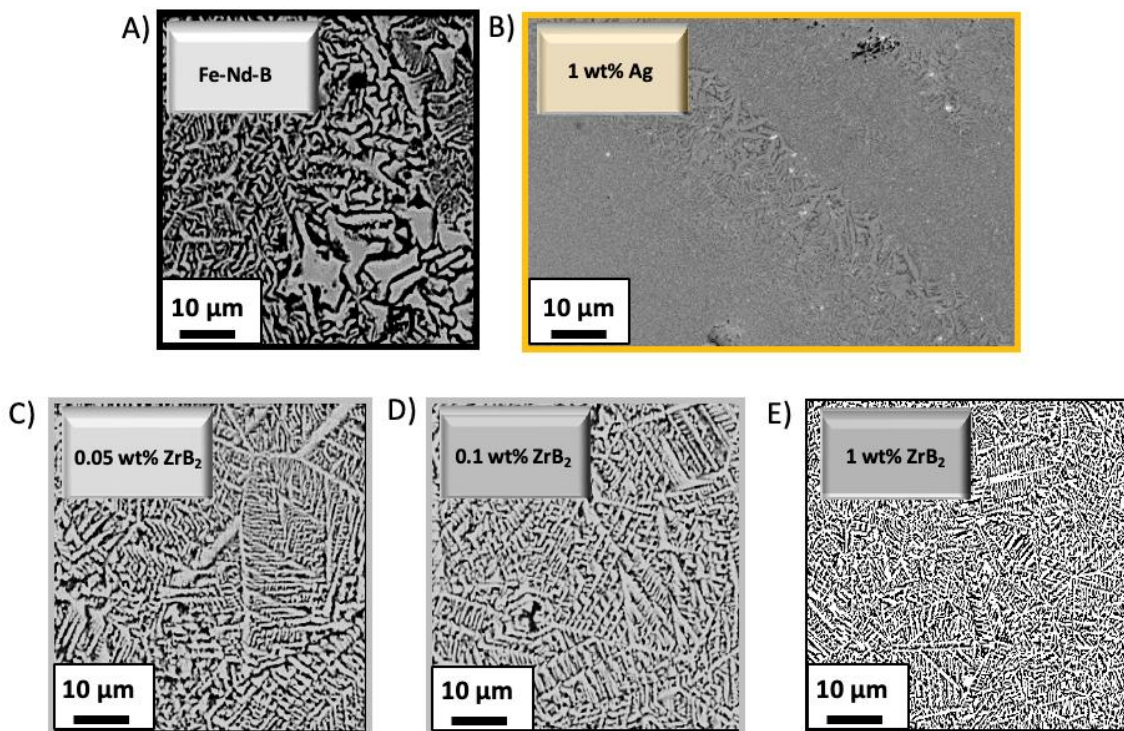


Figure 4: SEM-BSE images of annealed suction casting flakes from A) unmodified MQP-S feedstock, B) modified feedstock with 1 wt% Ag NPs, C) modified feedstock with 0.05 wt% ZrB<sub>2</sub> NPs, D) modified feedstock with 0.1 wt% ZrB<sub>2</sub> NPs, E) modified feedstock with 1 wt% ZrB<sub>2</sub> NPs.

Exemplary SEM-EDX mapping was performed to visualize the distribution of elements in the suction-casted parts (Figure 5), assessing their functionality. The focus was primarily on the samples containing 1 wt% Ag NPs or ZrB<sub>2</sub> NPs. Despite the very homogeneous Ag NPs distribution resulting after feedstock modification (Figure 2B), Ag was less uniformly distributed in the as-built part, with silver mostly concentrated on elevated regions, suggesting the presence of unmolten powder residues. However, the molten areas contained hardly any Ag or had amounts below the EDX's resolution limit.

Interestingly, areas with Ag had a significantly reduced percentage of Fe. Although it is unlikely for Ag to enter the Nd<sub>2</sub>Fe<sub>14</sub>B matrix, it could potentially form intermetallic phases

with Nd (not detected by EDX) <sup>21</sup>, which our study neither confirms nor negates. In comparison, Zr is wide and more evenly distributed in the cross-sections. As shown in Figure 5 D), due to the light color intensity (compared with Ag), no islands are observed. We cannot exclude that it stabilizes the Nd<sub>2</sub>Fe<sub>17</sub> phase simultaneously <sup>35</sup>, reducing functionality. It has to be noted here that since B could not be precisely detected from EDX, only Zr is tracked. It is insufficient to confirm whether the Zr is from NPs additivation or the original alloying element in the raw MQP-S powder.

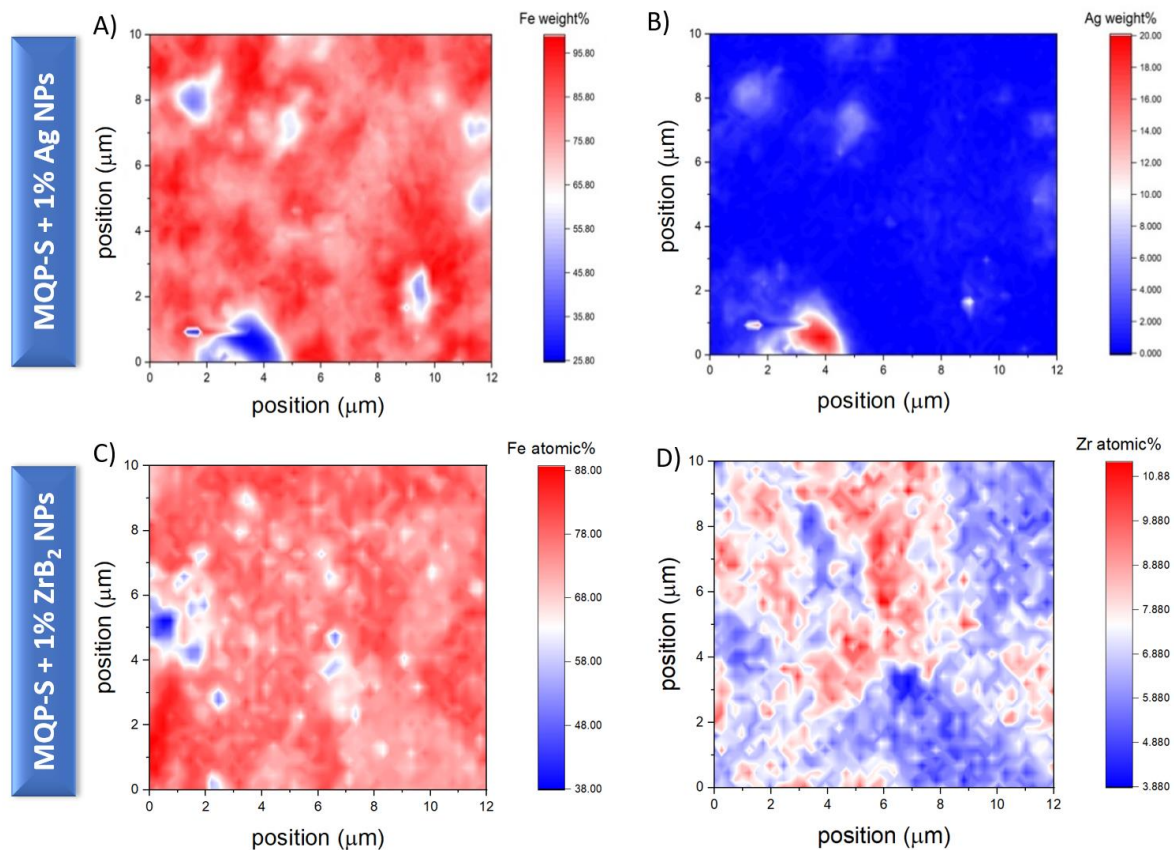


Figure 5: EDX mapping of annealed suction casting flakes made by the produced powder feedstocks. (A) and (B) show the mapping of elements Fe and Ag in the sample casted from Ag NP-decorated MQP-S powder; (C) and (D) show the mapping of elements Fe and Zr in the sample casted from ZrB<sub>2</sub> NP-decorated MQP-S powder.

As the microstructure is a decisive influence factor for the functionality of the MQP-S as build parts, we measured the magnetic properties using a vibrating sample magnetometer to reveal hysteresis loops. Figure 6 shows extracted magnetic properties (coercivity and remanence) for heat-treated suction-casted samples decorated with Ag NPs and ZrB<sub>2</sub> NPs in different mass loadings and compared to the respective values of the suction-casted pure MQP-S (orange). As expected from the literature <sup>22,33,36</sup>, the initial magnet material has totally lost its functionality showing a remanence of 0.29 T and a coercivity of less than 50 KA/m. Although

ZrB<sub>2</sub> shows a more homogeneous grain size distribution and dense dendritic structure, we do not observe any influence on the magnetic properties independent of the NPs mass loading. As mentioned above, we cannot exclude that Zr stabilizes Nd<sub>2</sub>Fe<sub>17</sub>, which is harmful to the hard magnetic properties and needs to be investigated for further studies. However, the Ag NPs ≥ 1 wt% show a huge impact on the functionality showing a 150% increase in coercivity and a 100% increase in remanence. Note that the remanence increases to 0.45 T, which is only 25 % below the physical limit of the material. For mass loadings exceeding 1 wt%, no statistically significant alteration has been detected. A mass loading of 1wt% seems to be the sweet spot for maximizing hysteresis via Ag NP additivation, corresponding to a feedstock surface load of only a half monolayer (see the sketch in Fig 6).

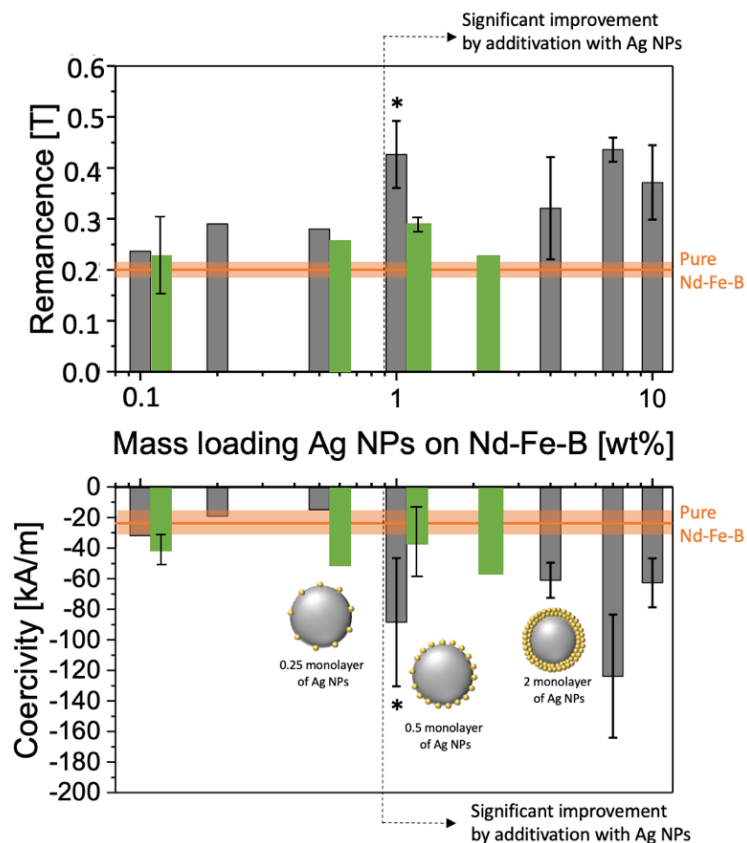


Figure 6: Extracted Remanence (A) and Coercivity (B) of the initial Fe-Nd-B feedstock (orange horizontal line), including data after supporting 1, 4, 10 wt% Ag NP, and 0.1, 0.5, 1, 2 wt% ZrB<sub>2</sub> NPson the microparticle surface. Data are collected after the suction casting of the produced powder feedstocks.

## Summary and Conclusion

In summary, we explored how modifying magnetic feedstock powders by low vol% of nanoparticles affects the microstructure and functionality of MQP-S after suction casting. Ag

and ZrB<sub>2</sub> were used as two different types of NPs. Ag NPs were expected to melt earlier and partly dissolve in the support material during processing, resulting in a more densely packed dendritic structure, smaller and more uniform grain sizes, and significantly increased functionality. In detail, an increase in coercivity of 150% and a 100% increase in remanence has been achieved. Interestingly, this effect was observed at loadings of only 0.7 vol% (geometrically equivalent to 0.5 monolayers of Ag NPs on the magnet microparticle surface). In contrast, ZrB<sub>2</sub> resulted in uniformly distributed grain sizes at much lower mass loadings with even more compact dendritic arms. However, no effect on functionality was observed, suggesting that the nanoparticles may be stabilizing phases harmful to hard magnetic functionality. Overall, surface additivation of 1 wt.% ligand-free silver nanoparticles on the magnet (MQP-S) micro powders strongly improves the hysteresis of permanent magnets after melting-fast-solidification processing, ready for testing in similar processes like laser powder bed fusion, in the future.

## Materials and Methods

This study used a gas-atomized Nd-Fe-B-based spherical powder manufactured by Neo Magnequench (Tuebingen, Germany). The powder is commercially known as MQP-S-11-9-20001 (hereafter referred to as MQP-S) with a declared chemical composition of Nd<sub>7.5</sub>Pr<sub>0.7</sub>Zr<sub>2.6</sub>Ti<sub>2.5</sub>Co<sub>2.5</sub>Fe<sub>75</sub>B<sub>8.8</sub> at%<sup>16,37</sup>. The powder size distribution and morphology were characterized by scanning electron microscopy (SEM, Philips ESEM-XL30 FEG, 20kV) equipped with an energy-dispersive X-ray detector (EDX) to evaluate the material composition and oxidation behavior. X-ray fluorescence (XRF, Bruker's S8 Tiger WD-XRF) measured the initial powder composition under inert gas conditions (He atmosphere). The true density of the powder was measured using a pycnometer (Borosilicate glass 3.3. DIN ISO 3507, BRAND 25 ml type Gay-Lussac).

The nano-additivation of the MQP-S powders is performed by adding laser-generated Ag NPs to the surface of the micrometer-sized MQP-S particles. The Ag NPs were prepared by laser ablation in liquids (LAL)<sup>24</sup>, where the laser ablated the surface of Ag-target (20mm (width) x 80mm (length) x 2mm(thickness)) immersed in water containing 0.1 µg/L NaOH stabilizer. Ag NPs were prepared using a ps-pulsed laser (500flex, Amphos GmbH, Herzogenrath, Germany)

with 150 W average output power. The fundamental wavelength was 1030 nm, with a laser pulse duration of 3 ps and a pulse repetition rate of 5 MHz. A galvanometer scanner (intelliSCAN-20, Scanlab AG, Purchheim, Germany) with a scanning speed of 5 m/s and an F-theta lens focusing optics  $f=254$  mm was employed. The hydrodynamic size of the synthesized Ag NPs was measured by analytical disc centrifugation (ADC, CPS instruments, INC) at a centrifugation speed of 24,000 rpm with a lower detection limit of 5 nm.

The MQP-S surface nano-functionalization was performed by directly mixing the powder with the colloid and post-processing to ensure the nanoparticle deposition, i.e. pH control and centrifugation. This methodology has been previously employed for the formation of heterogeneous catalysts<sup>38</sup> and the preparation of nano-functionalized steel powders to manufacture ODS steels by additive manufacturing techniques<sup>25</sup> The pH of the MQP-S-Ag colloid mixture was modified to pH 7.0 followed by centrifugation at 4000 rpm and 10° C for 15 minutes. After separating the nano-functionalized MQP-S powder and the supernatant, the powder is dried in a vacuum oven at 40 °C.

The prepared powder is processed by suction casting to emulate, with a lower powder amount, the high cooling rate and microstructure of PBF-LB processed samples. To prepare the powder for the suction casting system employed (Buehler MAM-1 arc melter), the Ag-MQP-S powder was pre-pressed into a copper crucible. An electric arc then melted the material, struck under a protective Ar atmosphere, and sucked into a water-cooled mold into bulk rectangular plates with a thickness of 0.5 mm. A heat treatment is applied to increase the coercivity of the manufactured parts. First, the samples are annealed at 1000 °C for 5 h with subsequent cooling in air. Then, a second annealing at 500 °C for 3 h is applied and the material is cooled down in the furnace. To determine the magnetic performance of the developed magnets, isothermal magnetization measurements were performed using a physical property measurement system (PPMS-VSM, Quantum Design PPMS-14) at room temperature under an applied magnetic field of up to 3 T.

To obtain grain orientation data, electron backscatter diffraction (EBSD) analyses were performed using a FEG-SEM (Tescan Mira3), operating at 30 kV with a step size of 0.1  $\mu\text{m}$ . For each sample, three maps with an area of 60 x 140  $\mu\text{m}^2$  were analyzed. A neighbor pattern averaging and re-indexing (NPAR<sup>®</sup>) post-processing routine was applied to improve the indexing rate using OIM Analysis 8.6 (EDAX) software.

## Acknowledgments

This work was financially supported by the Deutsche Forschungsgemeinschaft (DFG, German Research Foundation) within the Collaborative Research Centre / Transregio (CRC/TRR) 270, Project ID No. 405553726, subprojects A08, A10, A11, Z02.

## Conflicts of interest

The authors declare no conflicts of interest.

## References

1. Kok, Y., Tan, X. P., Wang, P., Nai, M. L. S., Loh, N. H., Liu, E., & Tor, S. B. Anisotropy and heterogeneity of microstructure and mechanical properties in metal additive manufacturing: A critical review. *Mater. Des.* **139**, 565–586 (2018), doi: 10.1016/j.matdes.2017.11.021.
2. DebRoy, T., Wei, H. L., Zuback, J. S., Mukherjee, T., Elmer, J. W., Milewski, J. O., Beese, A. M., Wilson-Heid, A., De, A. & Zhang, W. Additive manufacturing of metallic components – Process, structure and properties. *Prog. Mater. Sci.* **92**, 112–224 (2018), doi: 10.1016/j.pmatsci.2017.10.001.
3. Doñate-Buendía, C., Gu, D., Schmidt, M., Barcikowski, S., Korsunsky, A. M., & Goekce, B. On the selection and design of powder materials for laser additive manufacturing. *Mater. Des.* **204**, 109653 (2021), doi: 10.1016/j.matdes.2021.109653.
4. Kim, F. H. & Moylan, S. P. Literature review of metal additive manufacturing defects. *NIST AMS 100-16* (2018), doi:10.6028/NIST.AMS.100-16.
5. Trevisan, F., Calignano, F., Lorusso, M., Pakkanen, J., Aversa, A., Ambrosio, E. P., Lombardi, M., Fino, P. & Manfredi, D. On the Selective Laser Melting (SLM) of the AlSi10Mg Alloy: Process, Microstructure, and Mechanical Properties. *Materials* **10**, 76 (2017), doi: 10.3390/ma10010076.
6. Frazier, W. E. Metal Additive Manufacturing: A Review. *J. Mater. Eng. Perform.* **23**, 1917–1928 (2014), doi: 10.1007/s11665-014-0958-z.

7. Pauly, S., Wang, P., Kühn, U. & Kosiba, K. Experimental determination of cooling rates in selectively laser-melted eutectic Al-33Cu. *Addit. Manuf.* **22**, 753–757 (2018), doi: 10.1016/j.addma.2018.05.034.
8. Wu, A. S., Brown, D. W., Kumar, M., Gallegos, G. F. & King, W. E. An Experimental Investigation into Additive Manufacturing-Induced Residual Stresses in 316L Stainless Steel. *Metall. Mater. Trans. A* **45**, 6260–6270 (2014), doi: 10.1007/s11661-014-2549-x.
9. Kempen, K., Thijs, L., Van Humbeeck, J. & Kruth, J.-P. Mechanical Properties of AlSi10Mg Produced by Selective Laser Melting. *Phys. Procedia* **39**, 439–446 (2012), doi: 10.1016/j.phpro.2012.10.059.
10. Zyguła, K., Nosek, B., Pasiowiec, H. & Szysiak, N. Mechanical properties and microstructure of AlSi10Mg alloy obtained by casting and SLM technique. *World Sci. News* **104**, 456-466 (2018), EISSN 2392-2192.
11. Chaudhary, V., Mantri, S. A., Ramanujan, R. V. & Banerjee, R. Additive manufacturing of magnetic materials. *Prog. Mater. Sci.* **114**, 100688 (2020), doi: 10.1016/j.pmatsci.2020.100688.
12. Scheibel, F., Lauhoff, C., Riegg, S., Krooß, P., Bruder, E., Adabifiroozjæi, E., Molina-Luna, L., Böhm, S., Chumlyakov, Y. I., Niendorf, T. & Gutfleisch, O. On the Impact of Additive Manufacturing Processes on the Microstructure and Magnetic Properties of Co–Ni–Ga Shape Memory Heusler Alloys. *Adv. Eng. Mater.* **24**, 2200069 (2022), doi: 10.1002/adem.202200069.
13. Popov, V., Koptug, A., Radulov, I., Maccari, F. & Muller, G. Prospects of additive manufacturing of rare-earth and non-rare-earth permanent magnets. *Procedia Manuf.* **21**, 100–108 (2018), doi: 10.1016/j.promfg.2018.02.199.
14. Coey, J. M. D. *Magnetism and Magnetic Materials*, Cambridge university press (2010), ISBN: 9781139486927.
15. Schäfer, L., Skokov, K., Liu, J., Maccari, F., Braun, T., Riegg, S., Radulov, I., Gassmann, J., Merschroth, H., Harbig, J., Weigold, M. & Gutfleisch, O. Design and Qualification of Pr–Fe–Cu–B Alloys for the Additive Manufacturing of Permanent Magnets. *Adv. Funct. Mater.* **31**, 2102148 (2021), doi: 10.1002/adfm.202102148.
16. Skalon, M., Görtler, M., Meier, B., Arneitz, S., Urban, N., Mitsche, S., Huber, C., Franke, J. & Sommitsch, C. Influence of Melt-Pool Stability in 3D Printing of NdFeB Magnets on Density and Magnetic Properties. *Materials* **13**, 139 (2019), doi: 10.3390/ma13010139.

17. Goll, D., Vogelgsang, D., Pflanz, U., Hohns, D., Grubesa, T., Schurr, J., Bernthaler, T., Kolb, D., Riegel, H. & Schneider, G. Refining the Microstructure of Fe-Nd-B by Selective Laser Melting. *Phys. Status Solidi RRL - Rapid Res. Lett.* **13**, 1800536 (2019), doi: 10.1002/pssr.201800536.
18. Fidler, J. & Schrefl, T. Overview of Nd-Fe-B magnets and coercivity (invited). *J. Appl. Phys.* **79**, 5029 (1996), doi: 10.1063/1.361565.
19. Martin, J. H., Yahata, B. D., Hundley, J. M., Mayer, J. A., Schaedler, T. A. & Pollock, T. M. 3D printing of high-strength aluminium alloys. *Nature* **549**, 365–369 (2017), doi: 10.1038/nature23894.
20. Kusoglu, I. M., Vieth, P., Heiland, S., Huber, F., Lüddecke, A., Ziefuss, A. R., Kwade, A., Schmidt, M., Schaper, M., Barcikowski, S. & Grundmeier, G. Microstructure and corrosion properties of PBF-LB produced carbide nanoparticles additivated AlSi10Mg parts. *Procedia CIRP* **111**, 10–13 (2022), doi: 10.1016/j.procir.2022.08.046.
21. Zhao, T. S., Kim, Y. B. & Jeung, W. Y. Magnetic properties and microstructure of NdFeB sintered magnets by the addition of Ag powder. *IEEE Trans. Magn.* **36**, 3318–3320 (2000), doi: 10.1109/20.908784.
22. Goll, D., Trauter, F., Bernthaler, T., Schanz, J., Riegel, H. & Schneider, G. Additive Manufacturing of Bulk Nanocrystalline FeNdB Based Permanent Magnets. *Micromachines* **12**, 538 (2021), doi: 10.3390/mi12050538.
23. Jaćimović, J., Binda, F., Herrmann, L. G., Greuter, F., Genta, J., Calvo, M., Tomse, T. & Simon, R. A. Net Shape 3D Printed NdFeB Permanent Magnet: Net Shape 3D Printed NdFeB Permanent Magnet. *Adv. Eng. Mater.* **19**, 1700098 (2017), doi: 10.1002/adem.201700098.
24. Zhang, D., Gökce, B. & Barcikowski, S. Laser Synthesis and Processing of Colloids: Fundamentals and Applications. *Chem. Rev.* **117**, 3990–4103 (2017), doi: 10.1021/acs.chemrev.6b00468.
25. Doñate-Buendia, C., Kürnsteiner, P., Stern, F., Wilms, M. B., Streubel, R., Kusoglu, I. M., Tenkamp, J., Bruder, E., Pirch, N., Barcikowski, S., Durst, K., Schleifenbaum, J. H., Walther, F., Gault, B. & Gökce, B. Microstructure formation and mechanical properties of ODS steels built by laser additive manufacturing of nanoparticle coated iron-chromium powders. *Acta Mater.* **206**, 116566 (2021), doi: 10.1016/j.actamat.2020.116566.



26. Letzel, A., Maurer, E., Meixner, M., Poprawe, R., Stollenwerk, J., Hessner, S., Lehmann, K., Göckce, B. & Barcikowski, S. Effect of various dispersing agents on the stability of silver microparticle dispersion and the formulation of uniform silver film by laser melting. *J. Laser Appl.* **28**, 042004 (2016), doi: 10.2351/1.4955011.
27. Streubel, R., Wilms, M. B., Doñate-Buendía, C., Weisheit, A., Barcikowski, S., Schleifenbaum, J. H. & Gökce, B. Depositing laser-generated nanoparticles on powders for additive manufacturing of oxide dispersed strengthened alloy parts via laser metal deposition. *Jpn. J. Appl. Phys.* **57**, 040310 (2018), doi: 10.7567/JJAP.57.040310.
28. Rajendrachari, S., Swamy, B. E. K., Reddy, S. & Chaira, D. Synthesis of Silver Nanoparticles and their Applications. *Anal. Bioanal. Electrochem*, **5**, (2013).
29. Cao, R., Zhu, L., Liu, H., Yang, X., Nan, H., & Li, W. Improvement of corrosion resistance and magnetic properties for sintered NdFeB by alumina sol-containing conversion film. *RSC Adv.* **6**, 92510–92519 (2016), doi: 10.1039/C6RA19531H.
30. Gergoric, M. Hydrometallurgical Treatment of Neodymium Magnet Waste. Chalmers Tekniska Hogskola (Sweden) (2018), Order No. 27556747. ISBN 9781085761079.
31. Hupfeld, T., Sommereyns, A., Riahi, F., Doñate-Buendía, C., Gann, S., Schmidt, M., Gökce, B. & Barcikowski, S.. Analysis of the Nanoparticle Dispersion and Its Effect on the Crystalline Microstructure in Carbon-Additivated PA12 Feedstock Material for Laser Powder Bed Fusion. *Materials* **13**, 3312 (2020), doi: 10.3390/ma13153312.
32. Schäfer, L., Skokov, K., Maccari, F., Radulov, I., Koch, D., Mazilkin, A., Adabifiroozjaei, E., Molina-Luna, L. & Gutfleisch, O. A Novel Magnetic Hardening Mechanism for Nd-Fe-B Permanent Magnets Based on Solid-State Phase Transformation. *Adv. Funct. Mater.*, **33**(4), 2208821 (2023), doi: 10.1002/adfm.202208821.
33. Huber, C., Sepehri-Amin, H., Goertler, M., Groenefeld, M., Teliban, I., Hono, K. & Suess, D. Coercivity enhancement of selective laser sintered NdFeB magnets by grain boundary infiltration. *Acta Mater.* **172**, 66-71 (2019), doi: 10.1016/j.actamat.2019.04.037.
34. Lamichhane, T. N., Sethuraman, L., Dalagan, A., Wang, H., Keller, J. & Paranthaman, M. P. Additive manufacturing of soft magnets for electrical machines—a review. *Mater. Today Phys.* **15**, 100255 (2020), doi: 10.1016/j.mtphys.2020.100255.
35. Fayyazi, B. Novel magnetic materials by high-throughput reactive crucible melting, master thesis (2015) Materials Science, Technical University of Darmstadt, Alarich-Weiss-Str. 16, 64287 Darmstadt, Germany.

36. Bittner, F., Thielsch, J. & Drossel, W. G. Laser powder bed fusion of Nd–Fe–B permanent magnets. *Prog. Addit. Manuf.* **5**, 3–9 (2020), doi: 10.1007/s40964-020-00117-7.
37. Magnequench. Datasheet MQP-S-11-9-20001, this powder and its manufacturing processes are subject to one or more of the following United States Patents: 6,183,572; 6,478,890; 6,572,875; 6,855,265; 6,979,409; 7,087,185; 7,144,463 <https://mqqtechnology.com/product/mqp-s-11-9-20001/>.
38. Marzun, G., Nakamura, J., Zhang, X., Barcikowski, S. & Wagener, P. Size control and supporting of palladium nanoparticles made by laser ablation in saline solution as a facile route to heterogeneous catalysts. *Appl. Surf. Sci.* **348**, 75–84 (2015), doi: 10.1016/j.apsusc.2015.01.108.
39. Liang, S.-X., Zhang, L. C., Reichenberger, S. & Barcikowski, S. Design and perspective of amorphous metal nanoparticles from laser synthesis and processing. *Phys. Chem. Chem. Phys.* **23**, 11121–11154 (2021), doi: 10.1039/D1CP00701G.
40. Streubel, R., Barcikowski, S. & Gökce, B. Continuous multigram nanoparticle synthesis by high-power, high-repetition-rate ultrafast laser ablation in liquids. *Opt. Lett.* **41**, 1486 (2016), doi: 10.1364/OL.41.001486.
41. Fazio, E., Gökce, B., De Giacomo, A., Meneghetti, M., Compagnini, G., Tommasini, M., Waag, F., Lucotti, A., Zanchi, C. G., Ossi, P. M., Dell'Aglio, M., D'Urso, L., Condorelli, M., Scardaci, V., Biscaglia, F., Litti, L., Gobbo, M., Gillo, G., Santoro, M., Trusso, S. & Neri, F. Nanoparticles Engineering by Pulsed Laser Ablation in Liquids: Concepts and Applications. *Nanomaterials* **10**, 2317 (2020), doi: 10.3390/nano10112317.

## Supporting information

**Section I: Laser ablation in liquids process:** The technique of laser ablation in liquid (LAL) was first described by A. Fojtik and A. Henglein for simple and surfactant-free nanoparticle synthesis<sup>39</sup>. In contrast to wet chemical methods, laser synthesis does not demand the employment of chemical precursors and organic surfactants. LAL requires the delivery of a high energy density to the target material to overcome the ablation threshold and promote material removal from the target surface. The removed material is collected in the surrounding liquid forming a colloidal dispersion of nanoparticles. To overcome the ablation threshold while reducing the laser's interaction with the surrounding liquid, short and ultrashort laser pulses in the range of fs up to ns are employed instead of continuous wave lasers that suffer from strong heating of the liquid<sup>40</sup>. The LAL process outcome is

determined by various parameters, including material and laser features <sup>41</sup>. Another advantage of LAL is the reduction of byproducts in the colloids, allowing the direct employment of the generated nanoparticles without further purification steps. This is particularly appropriate for the Ag nanoparticles generated in the current work that is added to MQP-S powder by pH-controlled dielectrophoretic deposition. The process is proven to reduce nanoparticle agglomeration during nanoparticle support.

## **Section 2: Characterisation of the composition of MQP-S**

The composition of the initial feedstock powder was determined using XRF (see method section). The results are summarized in Figure S1. Note that the outcome differs slightly from the nominal composition near the stoichiometric  $\text{Nd}_2\text{Fe}_{14}\text{B}$ .

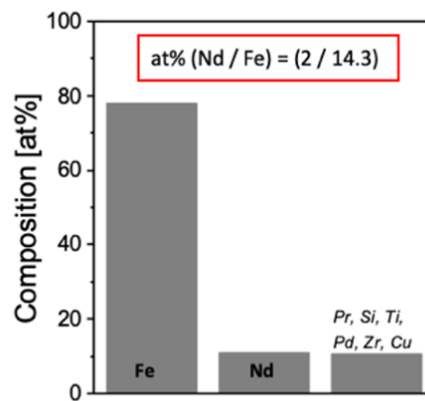


*Figure S1: Properties of non-additive MQP-S powder: A) chemical composition; B) half hysteresis loop with the initial magnetization curve.*

## **Section 3: Hysteresis loop of the unmodified feedstock after suction casting**

The experimental procedure of the suction casting process, incl. subsequent annealing steps, can be found in the method part. The hysteresis loop of the unmodified casted part is shown in Figure S2.

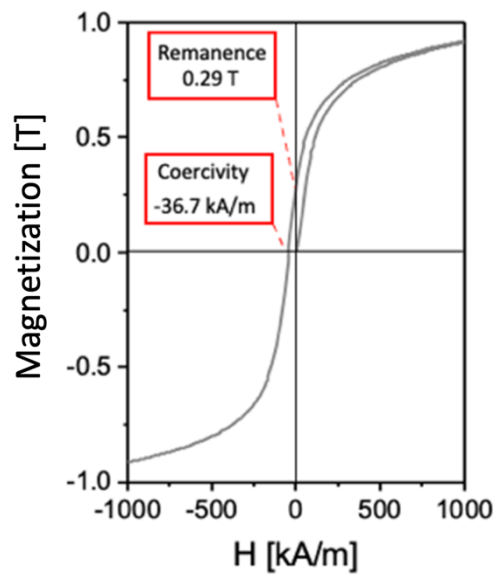


Figure S2: Hysteresis loop of the suction casted unmodified MQP-S feedstock after annealing.

#### Section 4: Surface modification step by colloidal nanoadditivation

Figure S3 shows SEM images of modified feedstocks with different NPs loading. With increasing Ag NP loading, the additives form island on the micro powder. Lower NPs loading, on the other hand, shows the NPs well dispersed on the microparticle surface.

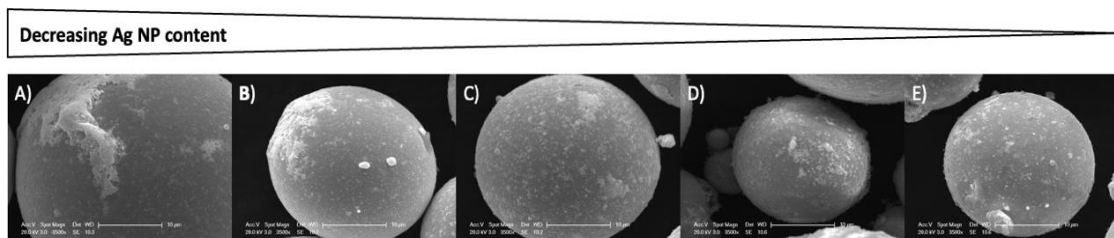
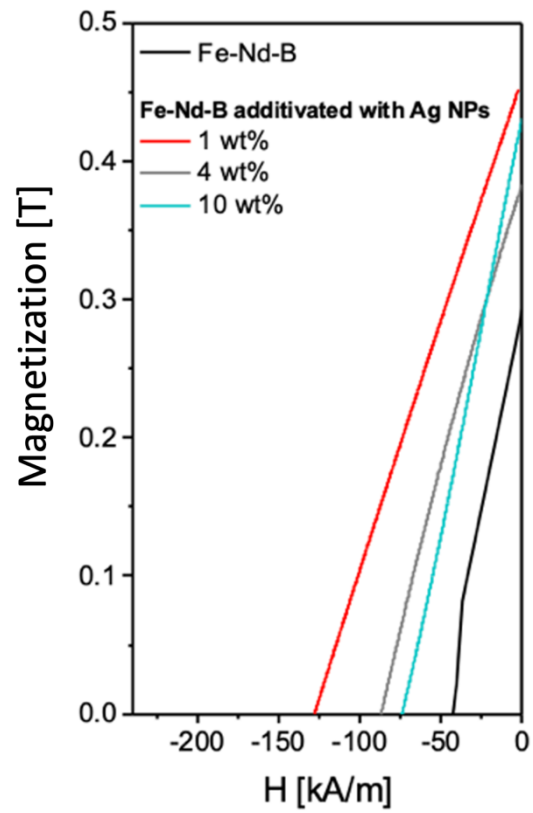


Figure S3: SEM images of Ag NPs modified powder with different mass loads. A) 5 wt% Ag NPs B) 2.5 wt% Ag NPs, C) 1 wt% Ag NPs D) 0.5 wt% Ag NPs E) 0.1 wt% Ag NPs.

**Section 5: Hysteresis behavior of modified feedstocks after suction casting.**



**Figure S 4:** Demagnetization curve of annealed suction casting flakes from non-modified powder and Ag NPs modified powder with the different mass loads.